Acceleration of ultrahigh-energy cosmic rays in the early afterglows of gamma-ray bursts: Concurrence of jet dynamics and wave-particle interactions

Ze-Lin Zhang, Ruo-Yu Liu,* and Xiang-Yu Wang†

School of Astronomy and Space Science, Nanjing University, Xianlin Road 163, Nanjing 210023, China and Key Laboratory of Modern Astronomy and Astrophysics, Nanjing University, Ministry of Education, Nanjing 210023, China

(Received 18 June 2021; accepted 4 October 2021; published 5 November 2021)

The origin of ultrahigh-energy cosmic rays (UHECRs) remains a mystery. It has been suggested that UHECRs can be produced by the stochastic acceleration in relativistic jets of gamma-ray bursts (GRBs) at the early afterglow phase. We develop a time-dependent model for proton energization by cascading compressible waves in GRB jets while considering the concurrent effect of the jet's dynamics and the mutual interactions between turbulent waves and particles. Considering the fast mode of a magnetosonic wave as the dominant particle scatterer and assuming the interstellar medium for the circumburst environment, our numerical results suggest that protons can be accelerated up to 10^{19} eV during the early afterglow. An estimation shows that ultrahigh-energy nuclei can easily survive photodisintegration in the external shocks in most cases, thus allowing the acceleration of 10^{20} eV cosmic-ray nuclei in the proposed frame. The spectral slope can be as hard as $dN/dE \propto E^0$, which is consistent with the requirement for the interpretation of the intermediate-mass composition of the UHECRs as measured by the Pierre Auger Observatory.

DOI: 10.1103/PhysRevD.104.103005

I. INTRODUCTION

Ultrahigh-energy cosmic rays (UHECRs) at the ankle energy $10^{18.5}$ eV and above are the most energetic particles in nature [1]. The presence of these particles has been known for over half a century [2]. However, the sites and mechanisms of their production are still open questions [3]. The study of the energy spectrum and the mass composition of the UHECRs helps reveal their origin. Recently, the results of cosmic-ray anisotropy observed by the Pierre Auger Observatory and the Telescope Array support the hypothesis of an extragalactic origin for the UHECRs [4,5]. Extragalactic sources, such as active galactic nuclei [6,7], gamma-ray bursts (GRBs) [8–10], energetic supernovae (such as hypernovae) [11,12], tidal disruption events [13–15], galaxy clusters [16–18], and millisecond magnetars [19,20], have been considered plausible candidates for UHECR sources.

As the most powerful and intense explosive events in the Universe, GRBs have been studied extensively as the cosmic accelerator of UHECRs [8–10,21–24]. However, the acceleration mechanisms of these particles in GRBs remain an enigma. The standard scenario adopted to produce nonthermal particles is the particle acceleration at shocks, e.g., diffusive shock acceleration [25,26]. However, particle acceleration by relativistic shocks with a bulk Lorentz factor $\Gamma \gg 1$ is limited by a series of factors. For example, the relative energy gain drops quickly (from Γ^2 to $\simeq 2$) after the first shock crossing circle because of particles do not have sufficient time to become isotropic upstream before being caught up by the shock (see, e.g., [27,28]; see also the recent review by Marcowith *et al.* [29]). Another possible disadvantage of the shock acceleration is the energy budget. The required energy production rate of CRs to explain the measured flux beyond the ankle is 10^{44} erg Mpc^{-3} yr^{-1} [30–32], while the gamma-ray energy production rate of GRBs is 10^{43} erg Mpc^{-3} yr^{-1} for a typical gamma-ray luminosity of 10^{52} erg s^{-1} and a local GRB rate of 1 Gpc^{-3} yr^{-1}. Given a predicted spectral slope of the accelerated particles of $p \gtrsim 2$ for the relativistic shock acceleration [33–36], the fraction of the energy of CRs accelerated beyond the ankle ($10^{18.5}$ eV) is only at a level of 10% of the total CR energy. As a result, it would require a baryon loading factor (defined as the ratio of total energy populated in CRs to that in gamma rays) of $\sim$100 to account for the required UHECR energy production rate. This is in tension with the constraint from the nondetection of GRB neutrinos by the IceCube neutrino telescopes in some dissipation mechanisms of GRBs [37]. Furthermore, it has been pointed out that a very hard CR injection

*ryliu@nju.edu.cn
†xywang@nju.edu.cn

spectrum with $p \lesssim 1$ is favored in order to fit the spectrum and composition of UHECRs measured by the Pierre Auger Observatory, where the best-fit index is even $p < 0$ [38,39].

Recently, a stochastic acceleration (SA) model of UHECRs via turbulence in GRB jets was proposed to avoid the problems mentioned above [23]. The SA can yield a hard UHECR spectrum with shallow index $p \lesssim 2$, which has been discussed as a possible charged particle acceleration mechanism in astrophysical plasmas [40–42]. Magnetohydrodynamic (MHD) turbulence is indispensable in various astrophysical processes. As the magnetic scattering centers in the SA scenario, MHD waves consist mainly of three types: incompressible Alfvén modes and compressible fast and slow modes [43]. Particle scattering and diffusion largely rely on the properties of the plasma turbulence. Fast mode waves show an isotropic cascade and could be the most effective scatterers of cosmic rays [44,45]. The spectrum of the isotropic cascade was claimed to be $k^{-3/2}$ [43].

The excitation of turbulence in plasmas generally stems from the anisotropy of particle distributions and MHD instabilities [46]. In our work, we consider the turbulence driven by MHD instabilities induced by the jet's propagation in the circumburst interstellar medium (ISM), such as Kelvin-Helmholtz, Rayleigh-Taylor, and Richtmyer-Meshkov instabilities [47–49]. The turbulence is injected at a scale comparable to the size of the shock and then cascades down to small scales due to the wave-wave interactions. We do not emphasize any specific instability while assuming that the turbulent magnetic field is of the same order of magnitude as the total magnetic field (in the relativistic limit, mainly contributed by fast mode waves under our assumption [45,50]). Charged particles are expected to be accelerated via the gyroresonance with MHD waves in the condition $\omega - k_{\parallel} v_{\parallel} = l\Omega_{\rm g}$ $(l = 0, \pm 1, \pm 2, \ldots)$, where $\omega = \pm k_{\parallel} v_{\rm w}$ is the wave frequency, $k_{\parallel}$ the parallel wave number, $v_{\rm w}$ the phase velocity, $v_{\parallel} = \mu v$ the particle velocity parallel to the mean magnetic field $B \equiv |\mathbf{B}|$, μ the pitch-angle cosine, and $\Omega_{\rm g}$ the gyrofrequency of relativistic particles. The positive and negative signs in the dispersion relation indicate the parallel and antiparallel propagation of waves to $\mathbf{B}$. In our work, we consider only the most important resonance occurring at $l = -1$ and $k_{\parallel} = \Omega_{\rm g}/v_{\parallel}$, which is generally true except for 90° scattering [51–53]. Notice that gyroresonance is not the only mechanism for wave-particle interactions in the MHD turbulence. For example, transit-time damping ($l = 0$ mode) can also contribute to particle scattering, especially when the pitch angle is close to 90° [54,55].

Asano and Mészáros [23] considered the SA process with a test-particle treatment and assumed nonevolving parameters such as the particle injection rate and the diffusion coefficient. In fact, acceleration of particles consumes the turbulence energy, represented as a damping process. In the meantime, it relaxes the confinement of particles in the jet and may cause particle escape from the jet. In addition, the GRB jet decelerates as it expands into the ISM. As a result, relevant parameters for the SA process evolve with time and particles that, confined in the jet, experience adiabatic cooling. These processes were not considered in Ref. [23], but they may significantly affect the SA process and, consequently, the accelerated CR spectrum.

In this work, we attempt to model the acceleration of UHECRs via the SA process in the early afterglow of GRBs with incorporating jet dynamics and the mutual influences between the particles and the turbulence. The configuration of this work proceeds as follows. In Sec. II, the gyroresonant interaction of wave and particle by coupled kinetic equations in the early afterglows of GRBs is introduced. In Sec. III, we analyze the acceleration of UHECRs by wave-particle interactions in a comprehensive way which covers the behaviors of the wave-particle spectra. In Sec. IV, we estimate the photodisintegration rate of ultrahigh-energy nuclei in the external shocks under the assumption of SA. Conclusions are presented in Sec. V. We use $\mathcal{Q}_x = \mathcal{Q}/10^x$ (i.e., $\mathcal{Q} = 10^{52}\mathcal{Q}_{52}$, except when $\mathcal{Q}_{300}$, in which case $\mathcal{Q}/300$) in cgs units throughout this work.

II. STOCHASTIC ACCELERATION IN THE EARLY AFTERGLOWS OF GRBs

For an isotropic-equivalent, adiabatic GRB ejecta expanding in ISM [56], the following equations have been proposed to depict its dynamic evolution [56]:

$$\frac{{\rm d}\Gamma}{{\rm d}m} \simeq -\frac{\Gamma^2 - 1}{M_{\rm ej} + 2\Gamma m}, \tag{1}$$

$${\rm d}m = 4\pi R^2 n_{\rm ISM} m_{\rm p} {\rm d}R, \tag{2}$$

$${\rm d}R = \beta_{\rm sh} c \Gamma (\Gamma + \sqrt{\Gamma^2 - 1}) {\rm d}t_{\rm obs}, \tag{3}$$

where Γ is the bulk Lorentz factor of the external shock and the initial bulk Lorentz factor is fixed at $\Gamma_0 = 300$. m and $M_{\rm ej}$ are the rest mass of the swept-up ISM and the mass ejected from the GRB central engine, respectively. R is the radius of the external shock; $n_{\rm ISM}$ is the number density of the interstellar medium; $m_{\rm p}$ is the mass of a proton; $\beta_{\rm sh} = v_{\rm sh}/c$, where $v_{\rm sh}$ is the bulk velocity of the material and c is the speed of light; and $t_{\rm obs}$ is the time measured in the observer's frame.

At the onset of the afterglow (external shocks) of GRBs, the relativistic outflowing plasma can excite large-scale turbulence by MHD instabilities. Particles in plasmas scatter off the randomly moving induced turbulence, which causes second-order Fermi acceleration [57]. After a period of "scattering," the transition from anisotropic particle velocity distribution to the isotropic one (actually, the scattering mentioned above is due to some collisionless

processes between particles and fast mode waves, such as gyroresonant wave-particle interactions [58]). Hence, the reduced momentum diffusion equation can be written as [42,59]

$$\frac{\partial f(p,t)}{\partial t}=\frac{1}{p^2}\frac{\partial}{\partial p}\left[p^2\mathcal{D}_{\rm pp}(p,t)\frac{\partial f(p,t)}{\partial p}\right], \tag{4}$$

where $f(p,t)$ is the phase space distribution function of momentum p and time t and $\mathcal{D}_{\rm pp}(p,t)$ is the momentum diffusion coefficient which represents the rate of interaction with the turbulent fields. We adopt the energy of particle E instead of its momentum p by invoking $f(p,t)=N(E,t)\mathrm{d}E/(4\pi p^2\mathrm{d}p)$. Furthermore, in consideration of the particle injection, escape, and adiabatic energy loss processes, the evolution of the proton energy distribution $N(E,t)$ in the outflowing plasma (jet) comoving frame can be described as follows by the Fokker-Planck (FP) equation [42,60]:

$$\frac{\partial N}{\partial t}=\frac{\partial}{\partial E}\left[\mathcal{D}_{\rm EE}(E,t)\frac{\partial N}{\partial E}\right]-\frac{\partial}{\partial E}\left[\left(\frac{2\mathcal{D}_{\rm EE}(E,t)}{E}+\langle\dot{E}\rangle\right)N\right]-\frac{N}{t_{\rm esc}}+\mathcal{Q}_{\rm inj}(E,t), \tag{5}$$

where $\langle\dot{E}\rangle=-E/t_{\rm ad}$ represents the adiabatic energy loss of relativistic expansion and $t_{\rm ad}=R/(\Gamma c)$ indicates the adiabatic energy loss timescale. The last term, $\mathcal{Q}_{\rm inj}(E,t)=\mathcal{Q}_0(t)\delta(E-E_{\rm inj})$, represents the continuous particle injection from the initial moment, $\mathcal{Q}_0(t)=4\pi R^2\Gamma n_{\rm ISM}c$ indicates the number density at the proton injection energy $E_{\rm inj}$, and we assume continuous injection of particles at $E_{\rm inj}=300\Gamma_{300}m_{\rm p}c^2$ during the early afterglow evolution, with $E=\Gamma m_{\rm p}c^2$ being the proton energy. The term $-N/t_{\rm esc}$ represents the spatial diffusive escape of the particle from the accelerated region, the size of which is R/Γ in the jet's comoving frame. The spatial diffusion coefficient $\mathcal{D}_{\rm RR}$ is related to the energy diffusion coefficient $\mathcal{D}_{\rm EE}$ by $\mathcal{D}_{\rm RR}\mathcal{D}_{\rm EE}=\beta_{\rm w}^2E^2$ when one omits the coefficient of order unity. Therefore, the escape timescale $t_{\rm esc}=R^2/\mathcal{D}_{\rm RR}=R^2/(\Gamma^2v_{\rm w}^2t_{\rm acc})$ [61], where $t_{\rm acc}=E^2/\mathcal{D}_{\rm EE}$ is the acceleration time for protons whose Larmor radii resonate with some character length scales of the turbulent magnetic fields, $v_{\rm w}$ is the phase speed of fast mode magnetosonic waves. The cooling effects owing to photopion production and proton synchrotron radiation can be neglected [23]. Without considering the adiabatic energy loss, we can combine the first two terms on the right-hand side of Eq. (5) into a single term $(\partial F_{\rm p}/\partial E)$ which represents the SA process. $F_{\rm p}$ can be written as

$$F_{\rm p}(E)=E^2\mathcal{D}_{\rm EE}(E)\frac{\partial}{\partial E}\left[\frac{N(E)}{E^2}\right]. \tag{6}$$

Since we deal with ultrarelativstic particles, the particle velocity $v\gg v_{\rm w}$ is considered in the numerical calculation. Hence, we use an approximated form of the diffusion coefficient in energy space given by [62,63]

$$\mathcal{D}_{\rm EE}(E)\sim\frac{E^2\beta_{\rm w}^2k_{\rm res}c}{r_{\rm g}u_{\rm B}}\int_{k_{\rm res}}^{k_{\rm max}}k^{-1}W_{\rm B}(k)\mathrm{d}k, \tag{7}$$

where the dimensionless speed is given by [64]

$$\beta_{\rm w}=\frac{v_{\rm w}}{c}=\sqrt{\frac{\hat{\gamma}P+B^2/4\pi}{\rho c^2+\hat{\gamma}P/(\hat{\gamma}-1)+B^2/4\pi}}, \tag{8}$$

$\hat{\gamma}=4/3$ represents the adiabatic index in the relativistic regime, $P=(4\Gamma^2n_{\rm ISM}m_{\rm p}c^2)/3$ is the relativistic gas pressure, $\rho=4\Gamma n_{\rm ISM}m_{\rm p}$ is the downstream rest mass energy density, and $n_{\rm ISM}$ is the upstream rest number density of protons. Without considering the damping effect on turbulent MHD waves, we find that the coefficient $\mathcal{D}_{\rm EE}\propto\beta_{\rm w}^2E^2c/(r_{\rm g}^{2-q}\lambda_{\rm max}^{q-1})$ is tested under different cases, such as $q=2$ (hard sphere approximation), $q=3/2$ (Kraichnan type), $q=5/3$ (Kolmogorov type), and $q=1$ (Bohm limit), and the spectral indices of the proton energy spectra $E^2N_{\rm CR}(E)$ are separately shown as 1, 3/2, 4/3, and 2, which is consistent with previous work [23,42,65]. The comoving magnetic field energy density will be calculated in Eq. (10), which satisfies

$$u_{\rm B}=\frac{B^2}{8\pi}=\int_{k_{\rm min}}^{k_{\rm max}}W_{\rm B}(k)\mathrm{d}k, \tag{9}$$

under the assumption that the magnitude of the initial magnetic field $B_0\simeq(32\pi\varepsilon_{\rm B}\Gamma_0^2n_{\rm ISM}m_{\rm p}c^2)^{1/2}$, and with $\varepsilon_{\rm B}$ being the magnetic field equipartition factor which indicates fraction of the magnetic field energy to the internal energy $\mathcal{E}_{\rm tot}$ (almost equal to the initial total energy of the GRBs). For highly turbulent plasma, we assume that the energy of the turbulent magnetic field is comparable to the total magnetic energy. The fast mode magnetosonic part $W_{\rm B}(k)=\alpha W(k)$ is the magnetic component of the total turbulent field energy density per unit wave number $W(k)$ (magnetic field plus plasma motion). Because it is still not clear what the portion of fast mode waves in relativistic MHD turbulence is, here we set the dimensionless parameter $\alpha=0.25$ [45]. Given the turbulent energy $\mathcal{E}_{\rm tur}=\varepsilon_{\rm T}\mathcal{E}_{\rm tot}$, where $\varepsilon_{\rm T}$ is the turbulence equipartition factor. $k_{\rm res}\equiv 1/r_{\rm g}(E)$ is the corresponding wave number of the wave resonating with protons of energy E, where $r_{\rm g}\simeq E/(eB)$ is the gyroradius (Larmor radius) of the protons. $k_{\rm min}$ and $k_{\rm max}$ represent, respectively, the minimum and the maximum

wave number of the turbulence which correspond to the injection eddy scale $\lambda_{\rm inj} = 2\pi/k_{\rm min}$ and the smallest eddy scale $\lambda_{\rm min} = 2\pi/k_{\rm max}$. Note that the injection eddy scale $\lambda_{\rm inj}$ should not be larger than the width of the shocked jet in the comoving frame R/Γ at the jet's radius R from the central engine. Hence, we use a dimensionless parameter ξ to parametrize the injection eddy scale $\lambda_{\rm inj} = \xi R/\Gamma \lesssim R/\Gamma$. The value of $\lambda_{\rm max}$ is rather trivial for our calculation as long as it is smaller than the gyroradius of the protons at injection, i.e., $2\pi r_{\rm g}(E_0)$. We here simply set it to 10^{16}cm.

The gyroresonant wave-particle interactions lead to energy exchange between the turbulent waves and particles. As we mentioned above, the MHD waves in relativistic jets are taken to be isotropic, and their spectral density $W(k,t)$ in wave-number space is determined as follows by the FP equation [66,67]:

$$\frac{\partial W}{\partial t} = \frac{\partial}{\partial k}\left[\mathcal{D}_{\rm kk}(k,t)\frac{\partial W}{\partial k}\right] - \frac{\partial}{\partial k}\left[\frac{2\mathcal{D}_{\rm kk}(k,t)}{k}W\right] + \frac{k}{3}(\nabla\cdot\mathbf{v})\frac{\partial W}{\partial k} + \Gamma_{\rm w}(k,t)W + \mathcal{Q}_{w,{\rm inj}}(k,t), \quad (10)$$

where the third term on the rhs of the equation represents the energy loss of the adiabatic expansion (i.e., $\nabla\cdot\mathbf{v} > 0$) of magnetic fields at different scales and $\mathbf{v}$ is the expansion velocity of the waves. $\Gamma_{\rm w}(k,t)$ represents the damping effect, and $\mathcal{Q}_{w,{\rm inj}}(k,t) = \mathcal{Q}_{\rm w0}(t)\delta(k-k_{\rm inj})$ represents the continuous energy injection into the turbulence at a monoscale $\lambda_{\rm inj} = 1/k_{\rm inj}$, where $\mathcal{Q}_{\rm w0} = 4\Gamma^2\varepsilon_{\rm T}n_{\rm ISM}m_{\rm p}c^2/(R/\Gamma c)$ is the injection rate per unit volume at the wave number $k_{\rm inj}$. As the jet's expansion, $k_{\rm inj}$ will gradually get smaller. Note that $k_{\rm inj}$ is not to be confused with another characteristic wave number $k_{\rm res,inj}$, which corresponds to the wave that is resonate with the protons at injection energy $E_{\rm inj}$. The first two terms on the right-hand side of Eq. (10) indicate the energy cascade process in the wave-number space, which can be reformulated in the same manner as Eq. (6) as $k^2\mathcal{D}_{\rm kk}(k)\partial/\partial k[W(k)/k^2]$.

Since we consider the compressible fast mode waves, the Iroshnikov-Kraichnan- (IK-) type turbulence is adopted, and the diffusion coefficient in wave-number space $\mathcal{D}_{\rm kk}(k)$ can be given by [67]

$$\mathcal{D}_{\rm kk}(k) = \mathcal{C}^2k^4v_{\rm w}\left[\frac{W(k)}{2u_{\rm B}}\right], \quad (11)$$

where $\mathcal{C}$ is the Kolmogorov constant of order unity. Note that turbulence could already be driven in the jet before the onset of the afterglow phase (i.e., during the prompt emission phase), so we assume the initial condition for $W(k,t)$ to be

$$W(k,t=0) \equiv \kappa_0 u_{\rm T}\left(\frac{k}{k_{\rm inj}}\right)^{-q}\exp\left(-\frac{k}{k_{\rm max}}\right), \quad (12)$$

where the parameter $\kappa_0 \approx -2k_{\rm inj}^q(k_{\rm max}^{-q+1} - k_{\rm inj}^{-q+1})$, $u_{\rm T} = 4\Gamma^2\varepsilon_{\rm T}n_{\rm ISM}m_{\rm p}c^2$ is the comoving turbulent field energy density, and the IK-type spectral index $q = 3/2$. Note that the damping effect, if not negligible, would cause the deviation of the turbulence spectrum from the IK spectrum.

The energy gain of particles serves as a damping process for the turbulence. We consider here only the damping of the turbulence due to the gyroresonance of the protons. Therefore, the energy dissipation rate of the turbulence should be equal to the energy gain rate of the protons [68], i.e.,

$$\int {\rm d}k\Gamma_{\rm w}(k)W(k) = -\int {\rm d}E E\frac{\partial F_{\rm p}(E)}{\partial E}. \quad (13)$$

From Eq. (7), integrating by parts twice, we obtain

$$\Gamma_{\rm w}(k) = -\frac{4\pi e^2\beta_{\rm w}^2 c}{k}\left[n(E_{\rm res}(k)) + \int_{E_{\rm res}(k)}^{E_{\rm max}}\frac{2n(E)}{E}{\rm d}E\right], \quad (14)$$

where $n(E) \equiv N(E)/V$ represents the number density and the volume of the acceleration zone in the jet's comoving frame is estimated using $V = 4\pi R^2\cdot R/\Gamma$. The turbulence at the wave number k is damped by protons with energy $E > E_{\rm res}(k)$, where $E_{\rm res} = eB/k$. The turbulent magnetic fields in the relativistic jet indicate that $\delta B \lesssim B$.

III. RESULTS AND DISCUSSIONS OF TURBULENT STOCHASTIC ACCELERATION

We adopt the Runge-Kutta method to solve the dynamical evolution of the GRB jet, and the central difference method to solve the time-dependent FP equations; see the appendix of Ref. [69] for details. UHECR protons accelerated by turbulence through wave-particle gyroresonant interactions are considered under four different cases, case I for $\xi = 0.1$ and $n_{\rm ISM} = 0.01$ cm^{-3}, case II for $\xi = 0.1$ and $n_{\rm ISM} = 1$ cm^{-3}, case III for $\xi = 1$ and $n_{\rm ISM} = 0.01$ cm^{-3}, and case IV for $\xi = 1$ and $n_{\rm ISM} = 1$ cm^{-3}. All these cases take the initial bulk Lorentz factor $\Gamma_0 = 300\Gamma_{300}$ and consider the onset of the afterglow at 0.1 s (in the observer's frame) after the burst such that the initial radius of the early afterglows are set to $R_0 \simeq 2\Gamma_0^2 ct_0 = 5.4\times10^{14}$ cm. The time-dependent proton spectra in these cases are shown in the upper panels of Figs. 1 and 2, where some relevant timescales are shown in the lower panels. Note that here we simply show the spectra in four typical moments. We present the spectra at more moments of the evolution in Appendix A.

By comparing the final spectra of the four cases, we can see that the maximum accelerated energy is roughly proportional to ξ, implying that the particle acceleration in the early afterglow is limited mainly by the eddy size or the longest wavelength of the turbulence. This agrees with the result in Ref. [23]. Considering the adiabatic cooling

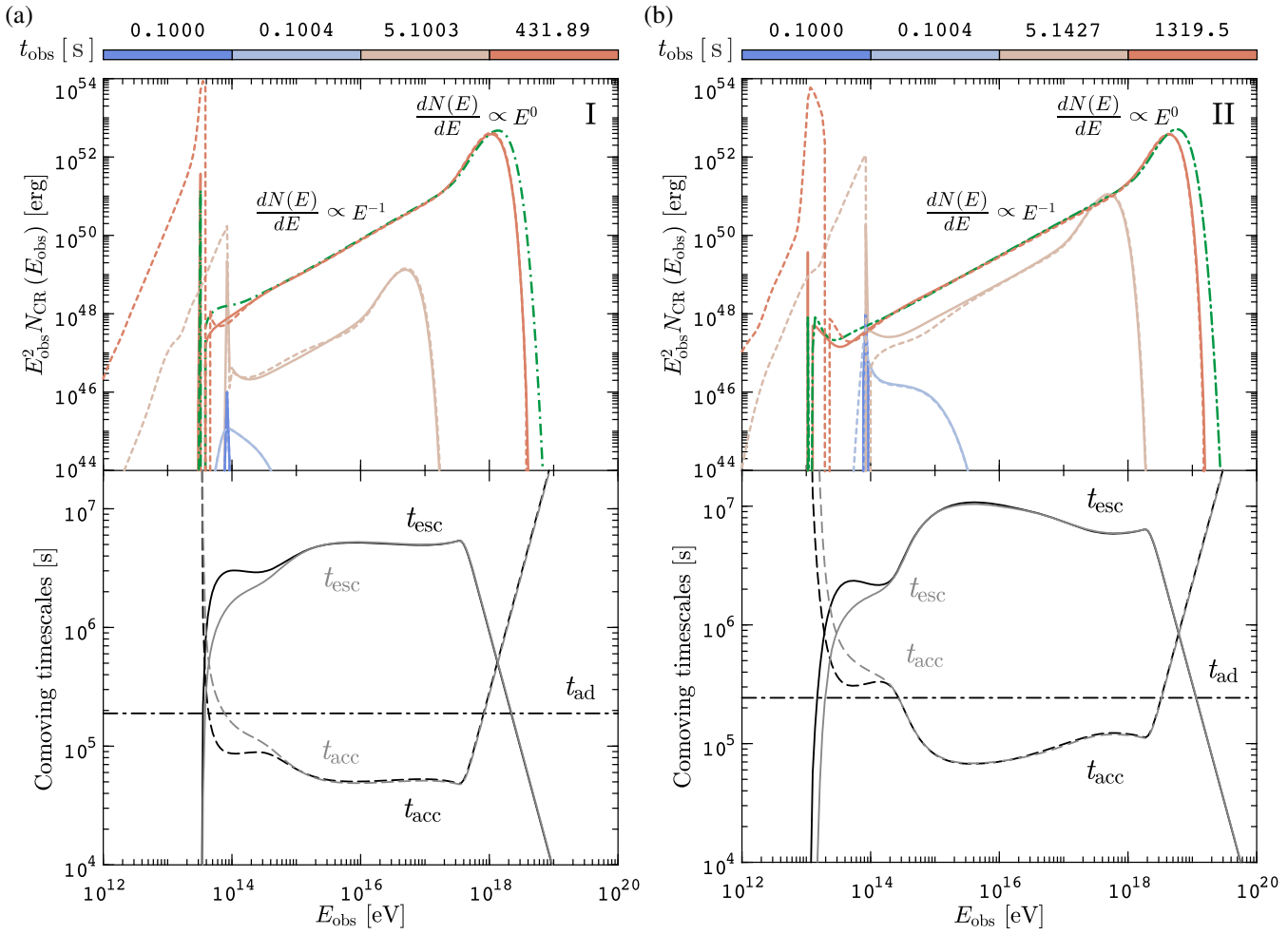

FIG. 1. UHECR proton spectra resulting from joint stochastic acceleration, particle diffusive escape, and adiabatic energy loss and their corresponding comoving timescales as a function of observed proton energy. Upper panels: dark blue lines represent the proton injection at 0.1000 s in the observer's frame. The color range of the solid lines progressing from dark blue to dark red represents the evolution of the proton spectrum in the case of $\xi = 0.1$. The corresponding colored short-dashed lines depict the evolution absent consideration of the particle spatial diffusive escape effect. The green dash-dotted lines in the upper panels delineate the cases in which one ignores the adiabatic energy loss at the final moment of the evolution. Lower panels: comoving timescales against the observed proton energy in the case of $\xi = 0.1$. The evolution of the energy spectra of protons for 100000 s in the comoving frame of relativistic outflowing plasma with $n_{\rm ISM} = 0.01$ cm^{-3} (case I) and $n_{\rm ISM} = 1$ cm^{-3} (case II). The acceleration, adiabatic expansion cooling, and diffusive escape timescales are separately denoted by dashed, dash-dotted, and solid lines. The gray lines show the evolution without inclusion of the adiabatic cooling process. Proton spectra evolve when (a) $t_{\rm obs} \in [0.1000\ {\rm s}, 431.89\ {\rm s}]$ and (b) $t_{\rm obs} \in [0.1000\ {\rm s}, 1319.5\ {\rm s}]$ in the observer's frame. We show only the final moment of the various timescales in the lower panels. More moments of the evolution of proton spectra are shown in Appendix A.

slightly softens the spectrum at the cutoff regime (where $t_{\rm acc} \simeq t_{\rm ad}$ or $E \simeq E_{\rm eq}$), as shown with the green dash-dotted lines. A smaller ξ, on the other hand, leads to a hardening or a pileup spectral feature at the high-energy end. This is because the same energy of turbulence would then distribute over a narrower span in the wave-number space given a smaller ξ, and hence enhance the energy density per unit wave number (i.e., there would be a larger $\mathcal{D}_{\rm EE}$). As a consequence, the SA process would push protons to higher energy more efficiently and, on the other hand, a smaller eddy size would result in the termination of wave-particle interactions at smaller energy. These two effects jointly lead to the formation of the pileup bump. The diffusive escape of particles does not have a significant influence on the spectrum at the high-energy end but plays an important role in shaping the spectrum around $E_{\rm inj}$, as shown in the upper panels of Figs. 1 and 2. The eddies around the resonant injection scale $\sim 1/k_{\rm res,inj}$ are largely consumed by the injected particles. Meanwhile, the number of scatterers (eddies) drops quickly, as particles can no longer be bound by waves. Therefore, particles can efficiently escape from the present acceleration region, causing the reduction of the

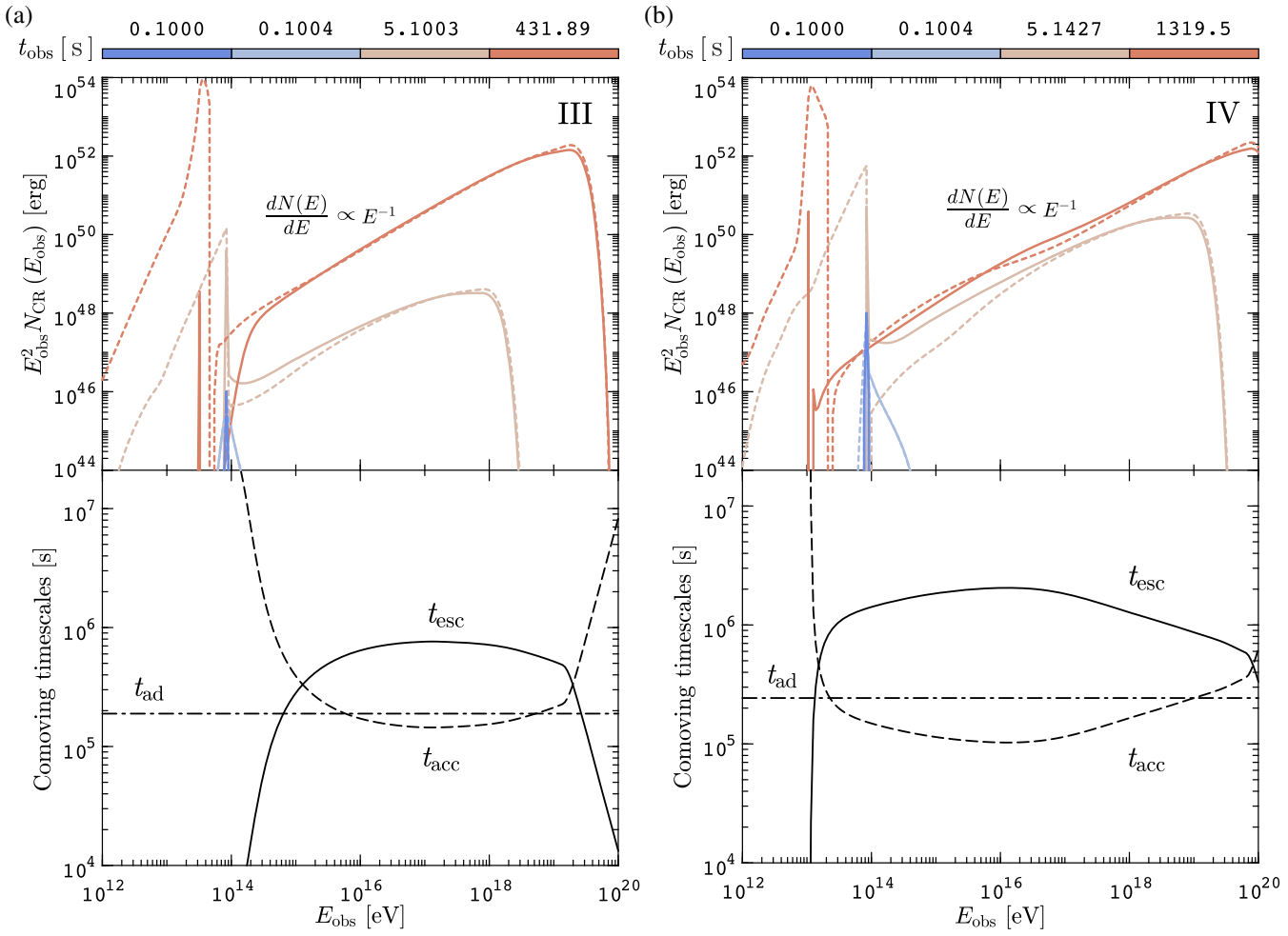

FIG. 2. Consistent with the descriptions in Fig. 1. Upper panels: lines ranging from dark blue to dark red represent the evolution of the proton spectrum in the case of $\xi = 1$. Lower panels: comoving timescales against the observed proton energy in the case of $\xi = 1$. The evolution of the energy spectra of protons for 100000 s in the comoving frame of relativistic outflowing plasma with $n_{\rm ISM} = 0.01$ cm^{-3} (case III) and $n_{\rm ISM} = 1$ cm^{-3} (case IV). For simplicity, here we simply compare the cases with and without the escape effect. More moments of the evolution of proton spectra are shown in Appendix A.

number of particles in the acceleration zone, as in the three cases (II–IV) shown in Appendix B, while the specificity of case I will be discussed separately below. This can be also seen by comparing the timescales shown in the lower panels of Figs. 1 and 2. At the high-energy end, when the acceleration timescale becomes comparable to the adiabatic cooling timescale (which is also comparable to the dynamical timescale), the diffusive escape timescale is still several times longer. In Fig. 1, we can see that the influence of the adiabatic cooling effect on the spectrum of the proton is not significant. As shown in the top panels of Fig. 1, it is worth noting that the total kinetic energy (or thermal energy in the rest frame if one assumes that swept-up protons are isotropized in the downstream of the shock) of the protons at injection is $\mathcal{E}_{\rm tot} \sim \Gamma^2 M_{\rm sw} c^2 \sim 10^{54}$ erg, where $M_{\rm sw}$ is the mass of swept-up material, but the protons are accelerated by extracting the turbulent magnetic field energy, and hence the total proton energy is restricted by the magnetic equipartition factor $\varepsilon_{\rm B} = \alpha \varepsilon_{\rm T}$. As a result, the baryon loading factor of accelerated protons is determined naturally instead of through manual selection. It should be noted that in order to ensure the validity of UHECR acceleration above the ankle in our model, the value of $\varepsilon_{\rm B}$ should not be much less than 0.1. For a local GRB rate of 1 Gpc^{-3} yr^{-1}, the required cosmic-ray energy budget should be about 10^{53} erg given the inferred CR energy production rate of 10^{44} erg Mpc^{-3} yr^{-1}. For GRBs with a typical total kinetic energy $\mathcal{E}_{\rm tot} = 10^{54}$ ergs, it would be insufficient to explain the origin of UHECRs with SA if $\varepsilon_{\rm B} \ll 0.1$.

Comparing Figs. 1 and 2, we observe that the maximum energy is also related to the ambient ISM density. At the early afterglow phase of GRBs, the jet has not been significantly decelerated so that the difference of the bulk Lorentz factor Γ. Therefore, the turbulence energy injection rate $\mathcal{Q}_{w,\rm inj}$ is proportional to the ambient gas density.

A higher ISM density converts more kinetic energy into magnetic energy, and hence a larger diffusion coefficient, which facilitates the acceleration, can be expected.

According to Ref. [42], if $q = 3/2$, the steady-state particle spectrum implied by Eq. (5) is $\mathrm{d}N/\mathrm{d}E \propto E^{1-q}$ when $E \in (E_{\rm inj}, E_{\rm eq})$, as long as the particle escape can be neglected $(t_{\rm esc} \gg t_{\rm acc},\ t_{\rm ad})$. Thus, the power-law energy spectra $E^2 N_{\rm CR}(E)$ is proportional to $E^{3/2}$. This is the result obtained in the test-particle limit and without considering the dynamic evolution of the system. In Figs. 1 and 2, we see that the bulk of the accelerated particle spectra in all four considered cases are softer. In general, when one takes the feedback of particle acceleration on the turbulence into account, the turbulence energy is consumed. Such a negative feedback from the protons impedes themselves to be further accelerated. The feedback is also reflected in the magnetic field strength, as can be seen in Fig. 3, where we compare the evolution of the magnetic field under the feedback with that expected in the standard GRB afterglow dynamic model. It is interesting to note that much of the previous literature found a very small $\varepsilon_{\rm B}$ for the external shock during modeling of the multiwavelength afterglow of some GRBs (see, e.g., Refs. [70–72]), which significantly deviates from the energy-equipartition value. We speculate that the feedback of the particle acceleration on the turbulence energy could be a reason. This will be studied elsewhere.

To show the tendency of energy transfer from turbulent magnetic field to particles, we compare the magnetic field energy density evolution under the four different cases, as shown in Fig. 3. Since the escape effect is considered in our model, the UHECR spectrum should be based on the escaped particles. If protons are confined in the shocked region, the protons lose energy via adiabatic cooling. The evolution time of the final UHECR spectra that escaped from the region should be longer than the deceleration time $t_{\rm dec}$. We know that the GRB jets start decelerating at a typical radius,

$$R_{\rm dec} \equiv \left(\frac{3E_{\rm tot}}{4\pi\Gamma_0^2 n_{\rm ISM} m_{\rm p} c^2}\right)^{1/3} \simeq 1.2\times10^{17} n_{\rm ISM}^{-1/3}\left(\frac{E_{\rm tot}}{10^{54}\,{\rm erg}}\right)^{1/3}\left(\frac{\Gamma_0}{300}\right)^{-2/3}\ {\rm cm}. \quad (15)$$

Therefore, in cases I and III, the deceleration radius $R_{\rm dec} \simeq 5.6\times10^{17}$ cm, and it is about 1.2×10^{17} cm in cases II and IV. Their corresponding deceleration timescales are $t_{\rm dec} \simeq 7.8\times10^4$ s and 1.7×10^4 s in the jet's comoving frame. To ensure that the final UHECR spectra escaped from the region after calculations longer than $t_{\rm dec}$, we set the evolution timescale of the wave-particle system in the jet's comoving frame $t_{\rm cmv} = 1.0\times10^5$ s, as shown in Fig. 3.

The evolution of turbulence energy and cosmic-ray energy are shown in the middle panels of Fig. 3. The turbulence energy is calculated as

$$\mathcal{E}_{\rm tur} = \Gamma V \int_{k_{\rm min}}^{k_{\rm max}} W(k)\mathrm{d}k, \quad (16)$$

and the corresponding cosmic-ray energy is given by

$$\mathcal{E}_{\rm CR} = \Gamma \int_{E_{\rm acc}}^{E_{\rm max}} E\frac{\mathrm{d}N(E)}{\mathrm{d}E}\mathrm{d}E \quad (17)$$

in the observer's frame. Here, $E_{\rm acc}$ is adopted as $5E_{\rm inj}$ for all cases. In cases III and IV, we can see that $\mathcal{E}_{\rm tur}$ is almost 10% of $\mathcal{E}_{\rm tot}$ $(\varepsilon_{\rm T} = 0.1)$ in the equilibrium state, and the cosmic-ray energy which is extracted from the fast mode waves energy is about 25% to $\mathcal{E}_{\rm tur}$ $(\alpha = 0.25)$. However, in cases I and II, we can see that $\mathcal{E}_{\rm tur}$ is only slightly larger than $\mathcal{E}_{\rm CR}$. Owing to the smaller $\xi = 0.1$ in cases I and II, the position of resonant injection wave number $k_{\rm res,inj}$ is closer to the injection wave number $k_{\rm inj}$ (higher energetic waves), as shown in cases I and II of Fig. 5 in Appendix A. We noticed that the magnitudes of the turbulent magnetic fields in cases III and IV (conservation of the turbulent magnetic field is well maintained) are almost twice those in cases I and II during the evolution. This means that protons get twice as much energy in cases I and II than in cases III and IV. With fewer scatterers, these energized protons are more likely to escape from the acceleration region, and this is the case, as shown in Fig. 6 in Appendix B. The turbulence energy in cases I and II is half that of cases III and IV. The reason for this is that damping of waves occurs even at the wave injection scale $\sim k_{\rm inj}$.

In addition, we noticed that the complex behavior of case I is related to the relative values between $k_{\rm inj}$ and $k_{\rm res,inj}$. A detailed explanation of it is given in Appendix C. In the meanwhile, our model requires that the wave number k should not be less than the injection wave number $k_{\rm inj}$, as shown in the final moment of evolution of Fig. 4. However, the diffusive nature of the FP equation allow the existence of wave numbers smaller than $k_{\rm inj}$. In our calculation of the turbulent magnetic field, the distribution of wave numbers $k < k_{\rm inj}$ is omitted. Hence, we get a relatively small value for the turbulent magnetic field in the case with $\xi = 0.1$.

Furthermore, the magnetic energy is also lost due to the adiabatic expansion of the jet. Since we assume the injection eddy size to be proportional to the jet's radius, the expansion of the jet also reduces the injection wave number of the turbulence $k_{\rm inj}$. The turbulent energy would then distribute over a larger and larger range in the wave number space, so the energy density per wave number is reduced. Therefore, relative to the case in the test-particle limit and the steady state, there will be a decline in the capacity of the SA with time. This is also reflected in the particle spectrum.

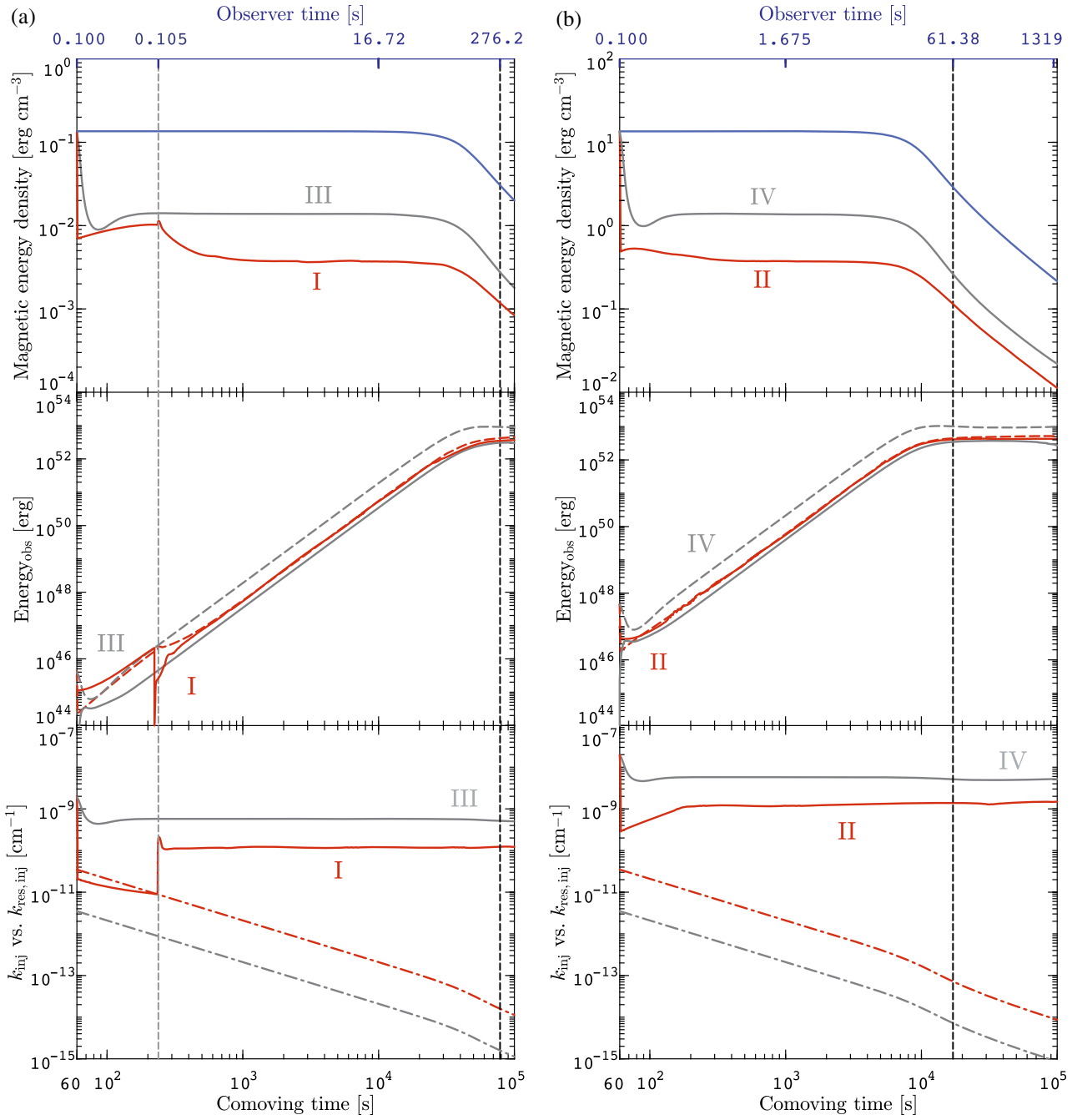

FIG. 3. Top panels: evolution of the magnetic field energy density in the phase of the GRB's early afterglows which are under the four different cases. The blue solid lines represent the evolution of the magnetic field energy density in the GRB blast wave (downstream of the shocked fluid) without consideration of the wave-particle interactions calculated with $B \simeq \sqrt{32\pi\epsilon_B\Gamma^2 n_{ISM} m_p c^2}$. (a) $n_{ISM} = 0.01$ cm^{-3}. (b) $n_{ISM} = 1$ cm^{-3}. The colored solid lines (gray for $\xi = 1$ and red for $\xi = 0.1$) show the evolution of the magnetic energy density components (without fast mode waves which are consumed by protons) of the turbulent magnetic fields with damping by protons are calculated using Eq. (9). The black dashed lines represent the deceleration time. Middle panels: The evolution of turbulence energy (dashed lines) and cosmic-ray energy (solid lines) in the observer's frame. Bottom panels: injection wave number k_{inj} (dash-dotted lines) and resonant injection wave number $k_{res,inj}$ (solid lines). The vertical gray dashed line represents the moment when $k_{inj} = k_{res,inj}$ again.

We can see that the bulk of the accelerated particle spectrum is softer than $E^{3/2}$.

According to the above parameter evolution, the shape of the wave energy density spectra can be easily determined from two types of wave numbers, k_{inj} and $k_{res,inj}$, as shown in Figs. 3 and 4. As the turbulent eddy scale becomes larger and larger, its wave number becomes smaller and smaller. Eddies associated with larger wave numbers

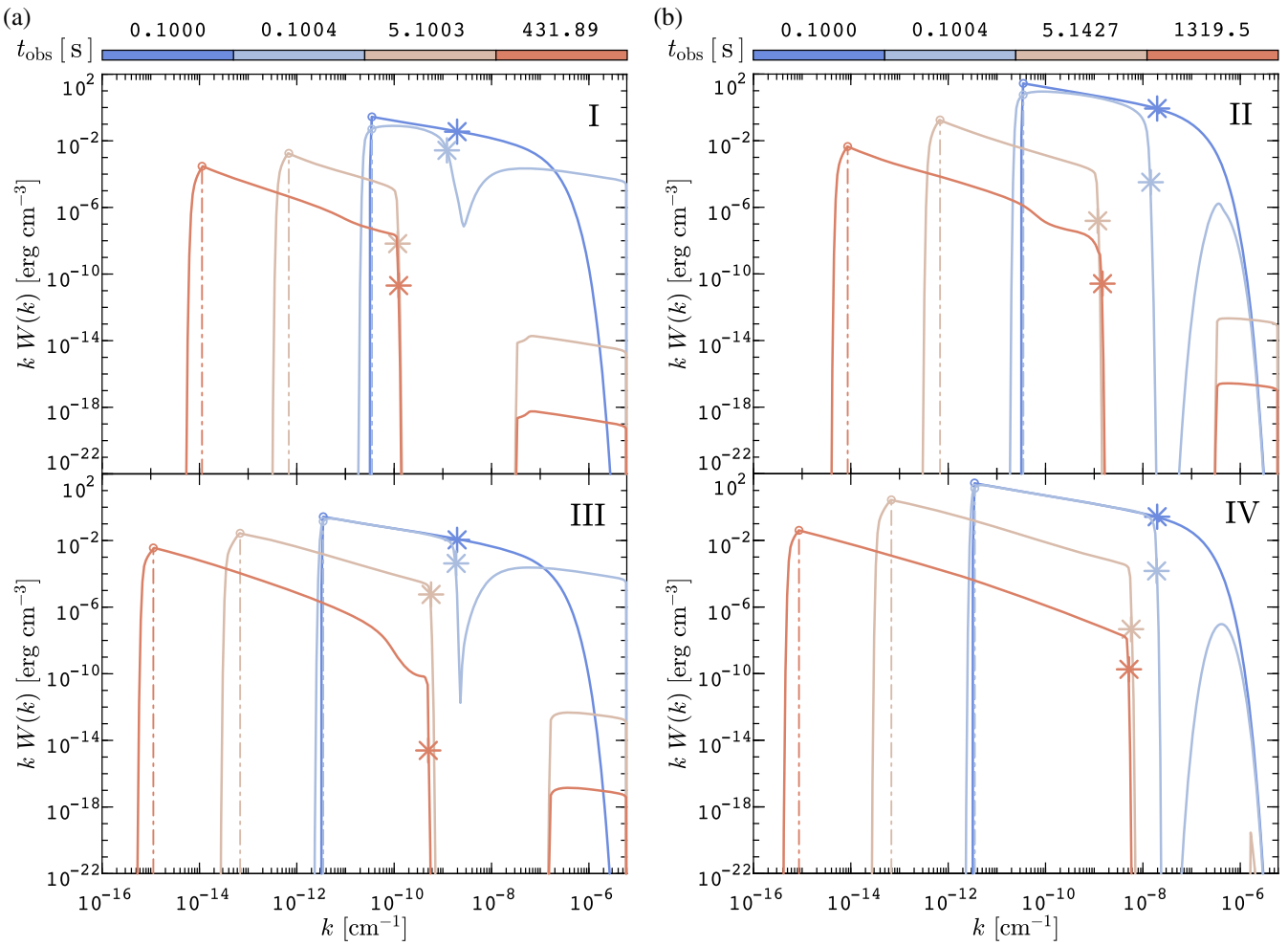

FIG. 4. Turbulence spectral energy density against wave number. The initial wave energy (magnetic field plus plasma motion) injection at 0.1000 s in the observer's frame is distinctly represented by the dark blue solid lines in the upper panels ($\xi = 0.1$) and lower panels ($\xi = 1$). Solid lines ranging in color from dark blue to dark red represent the evolution of the turbulent waves in the cases of $\xi = 0.1$ (cases I and II) and $\xi = 1$ (cases III and IV). The evolution of the relativistic outflowing plasma wave spectra for $t_{\rm cmv} = 100000$ s with $n_{\rm ISM} = 0.01$ cm^{-3} (left panels) and $n_{\rm ISM} = 1$ cm^{-3} (right panels). Evolution time is shown for (a) $t_{\rm obs} \in [0.1000\ {\rm s}, 431.89\ {\rm s}]$ and (b) $t_{\rm obs} \in [0.1000\ {\rm s}, 1319.5\ {\rm s}]$ in the observer's frame. Asterisks on the lines show the turbulent magnetic field energy density which are corresponding to the wave number $k_{\rm res,inj}$. The circles at different moments show the injected position of turbulent waves. The dash-dotted lines represent the cutoff position of the injection wave number at different moments. More moments of the turbulence spectra are shown in Appendix A.

(smaller scales) have already been damped by the corresponding lower-energy particles, the relatively higher-energy particles trapped in the acceleration region which can continuously gain energy from the lower-wave-number turbulent waves. Then energy transport in k space will cause a more remarkable deviation from the IK-type spectrum at lower wave numbers.

In the case of the ISM environment around bursts, our results suggest that a combination of cyclotron wave damping and gyroresonant particle acceleration in the early afterglows of GRBs could account for the origin of UHECRs. It is worth noting that the evolution of the jet's expansion can reduce the acceleration capacity of turbulence due to the dilution and adiabatic loss of the magnetic energy. In other words, the fluctuating magnetic field can energize cosmic rays more efficiently without considering the evolution of the jet's dynamics. For convenience, we list in Table I some parameters and their implications in the numerical calculation. Note that here we simply show the spectra at four typical moments. We present the spectra at more moments of the evolution in Appendix A.

It is worth mentioning that, as an equally important component of the turbulent plasma, electrons might express nonthermal radiation processes in the early afterglows of GRBs. We believe that the electron acceleration in the frame of SA has the value in itself [73]. For example, a study of SA of electrons in a scenario with prompt emission of GRBs has been carried out to explain the origin of the

TABLE I. The list of key parameters in numerical calculation. In the value column, each long dash represents a set of data.

Parameter (units)	Definition	Value (cases)	
ξ ($\oslash$)[a]	Dimensionless eddy scale	0.1 (I, II)	1 (III, IV)
$n_{\rm ISM}$ ($\rm cm^{-3}$)	Number density of the homogeneous medium	0.01 (I, III)	1 (II, IV)
B_0 (G)	Initial magnetic field	1.84 (I, III)	18.4 (II, IV)
$R_{\rm dec}$ (cm)	Deceleration radius (in comoving frame)	5.6×10^{17} (I, III)	1.2×10^{17} (II, IV)
$t_{\rm dec}$ (s)	Deceleration time (in comoving frame)	7.8×10^{4} (I, III)	1.7×10^{4} (II, IV)
α ($\oslash$)	Magnetic component of the total turbulent field	0.25 (I–IV)	
$\mathcal{C}$ ($\oslash$)	Kolmogorov constant from Eq. (11)	1 (I–IV)	
$\mathcal{E}_{\rm tot}$ (erg)[b]	Total isotropic kinetic energy	10^{54} (I–IV)	
$\varepsilon_{\rm B}$ ($\oslash$)	Magnetic field equipartition factor	0.025 (I–IV)	
$\varepsilon_{\rm T}$ ($\oslash$)	Equipartition factor of turbulent waves to $E_{\rm tot}$	0.1 (I–IV)	
Γ_0 ($\oslash$)	Initial bulk Lorentz factor	300 (I–IV)	
R_0 (cm)	Initial radius of the jet's evolution	5.4×10^{14} (I–IV)	
t_0 (s)[c]	Initial time of the jet's evolution	60 (I–IV)	
$\mathcal{D}_{\rm EE}$ ($\rm eV^2\,s^{-1}$)	Diffusion coefficient in energy space	—(I–IV)[d]	
$\mathcal{D}_{\rm kk}$ ($\rm cm^{-2}\,s^{-1}$)	Diffusion coefficient in wave-number space	—(I–IV)	
$\Gamma_{\rm w}$ ($\rm s^{-1}$)	Damping rate of the cascading turbulent waves	—(I–IV)	
$k_{\rm res,inj}$ ($\rm cm^{-1}$)	Resonant injection wave number	—(I–IV)	
$k_{\rm inj}$ ($\rm cm^{-1}$)	Injection wave number	—(I–IV)	
$W(k)$ ($\rm erg\,cm^{-2}$)	Total turbulence energy density per unit wave number	—(I–IV)	
$W_{\rm B}(k)$ ($\rm erg\,cm^{-2}$)	Fast magnetosonic mode component of $W(k)$	—(I–IV)	

[a]Dimensionless physical parameter.
[b]The initial energy of the burst measured by an observer is $\mathcal{E}_{\rm tot}=\Gamma_0 M_{\rm ej}c^2$.
[c]At the phase of early afterglow, begin with 0.1 s after the burst in the frame of the central engine.
[d]"—" means a set of data.

Band function [74]. However, the focus of this work is on UHECR acceleration. The study of electron SA in the framework of our model will be studied in the near future.

IV. PHOTODISINTEGRATION OF UHECRS IN THE STOCHASTIC ACCELERATION SCENARIO

Information about the energy loss processes of nuclei can provide important clues as to the mass composition of accelerated particles. An ultrahigh-energy nucleus with Lorentz factor $\Gamma_{\rm A}$ traveling through an isotropic photon background with number density $n_\gamma(\varepsilon_\gamma){\rm d}\varepsilon_\gamma$ in the energy range $(\varepsilon_\gamma,\varepsilon_\gamma+{\rm d}\varepsilon_\gamma)$ suffers from a loss of nucleons through the photodisintegration process, and the reaction rate is given by [75]

$$t_{\rm dis}^{-1}=\frac{c}{2\Gamma_{\rm A}^2}\int_{\varepsilon_{\rm th}}^{\infty}\sigma_{\rm dis}(\varepsilon'_\gamma)\varepsilon'_\gamma{\rm d}\varepsilon'_\gamma\int_{\varepsilon'_\gamma/2\Gamma_{\rm A}}^{\infty}\frac{n_\gamma(\varepsilon_\gamma)}{\varepsilon_\gamma^2}{\rm d}\varepsilon_\gamma, \tag{18}$$

where $t_{\rm dis}$ represents the photodisintegration energy loss time, while ε'_γ and ε_γ are the photon energies in the nucleus rest frame and lab frame, respectively. The dominant channel of this process is called giant dipole resonance (GDR). The relevant threshold energy $\varepsilon_{\rm th}=10$ MeV and the cross section in the energy range $\varepsilon'_\gamma\in(\varepsilon_{\rm th},30\ {\rm MeV})$ with loss of a single nucleon can be roughly described in a Lorentzian form [76] as

$$\sigma_{\rm dis}(\varepsilon'_\gamma)=\frac{\sigma_0\varepsilon'^2_\gamma\Delta^2_{\rm GDR}}{(\varepsilon_0^2-\varepsilon'^2_\gamma)^2+\varepsilon'^2_\gamma\Delta^2_{\rm GDR}}, \tag{19}$$

where σ_0 and $\Delta_{\rm GDR}$ are the maximum value and width of the cross section with the peak energy ε_0. The numerical fitting values are $\sigma_0=1.45\ A\times10^{-27}\ {\rm cm}^2$, $\Delta_{\rm GDR}=8$ MeV, and $\varepsilon_0=42.65\ A^{-0.21}$ MeV for $A>4$ [77]. Equation (19) is adequate for soft photon spectra, although a power-law function is more reasonable for the energy distribution of photons. However, for simplicity, we choose the delta function approximation $\sigma_{\rm dis}(\varepsilon'_\gamma)\sim\sigma_0\Delta_{\rm GDR}\delta(\varepsilon'_\gamma-\varepsilon_0)$ to estimate the reaction rate (the results of estimation of these two methods are in the same order of magnitude; we can see that it will not affect our conclusion about the photodisintegration of heavier nuclei).

The accelerated ultrahigh-energy nuclei with energies $\varepsilon_{\rm obs}$ above 10^{19} eV prefer to interact with these x-ray photons if the shock's Lorentz factor $\Gamma\in(10^2,10^3)$, and the Lorentz factor of an ultrahigh-energy nucleus $\Gamma_{\rm A}=\varepsilon_{\rm obs}/(A\Gamma m_{\rm p}c^2)$ in the observer's frame. Assuming that the spectrum of the early x-ray afterglow follows the fast-cooling behavior with $F_\nu\sim\nu^{-1}$ [78], we can get the following photodisintegration rate of a nucleus moving with $\Gamma_{\rm A}$ [79]:

$$t_{\rm dis}^{-1}=\frac{4}{3}c\sigma_0\frac{\Delta_{\rm GDR}}{\varepsilon'_0}\frac{\Gamma_{\rm A}U_{\rm X}}{\kappa\varepsilon'_0}, \tag{20}$$

where $U_X = \kappa n_b(\varepsilon_b)\varepsilon_b^2$ is the comoving-frame energy density of x-ray afterglow photons and ε_b is the break energy, $\kappa = \ln(\varepsilon_{BAT,+}/\varepsilon_{BAT,-}) \simeq 3$, with $\varepsilon_{BAT,+}$ and $\varepsilon_{BAT,-}$ being the upper and lower end of *Swift*–Burst Alert Telescope (BAT) energy threshold. In the early phase of the external shock for a GRB with bright x-ray afterglow emission, such as GRB 190114C [80], the average luminosity of the relevant x-ray afterglow observed by *Swift*-BAT is about $L_X = 4\pi R_{ex}^2 \Gamma^2 c U_X \simeq 10^{48.5}$ erg s^{-1} during the initial $\sim 68 - 110$ s, where R_{ex} is the radius of the external shock at the final stage of the free expansion phase of the turbulent ejecta. For ultrahigh-energy nuclei, the effective optical depth $\tau = t_{dyn}/t_{dis}$ for photodisintegration with the four cases mentioned above at $t_{obs} \simeq 80$ s are given by

$$\begin{cases} 6.5 \times 10^{-5} L_{X,48.5} E_{obs,18} R_{ex,17.5}^{-1} \Gamma_{249}^{-4} (A/56)^{0.42} & \text{I} \\ 6.5 \times 10^{-4} L_{X,48.5} E_{obs,19} R_{ex,17.5}^{-1} \Gamma_{249}^{-4} (A/56)^{0.42} & \text{III} \\ 9.1 \times 10^{-3} L_{X,48.5} E_{obs,18.5} R_{ex,17.1}^{-1} \Gamma_{123}^{-4} (A/56)^{0.42} & \text{II} \\ 9.1 \times 10^{-2} L_{X,48.5} E_{obs,19.5} R_{ex,17.1}^{-1} \Gamma_{123}^{-4} (A/56)^{0.42} & \text{IV} \end{cases} . \quad (21)$$

From the above results, we conclude that for all four cases the ultrahigh-energy nuclei (iron) can easily survive photodisintegration. From the Hillas criterion [81], we know that the maximum energy of UHECR is $E_{max} \propto AeBl$, where l is the scale of the acceleration region. As long as ultrahigh-energy nuclei survive photodisintegration, heavier nuclei can achieve a higher maximum energy.

V. CONCLUSIONS

In this paper, we took into account the concurrence of GRB jet dynamics and the kinetic descriptions of wave-particle interactions including SA process of particles and the damping of MHD fast mode waves. Protons can be accelerated to ultrahigh energy by turbulent waves through wave-particle gyroresonant interactions.

Including the evolution of a jet's dynamics can reduce the energy density of the turbulent magnetic fields and subsequently weaken the capacity of the acceleration of the SA mechanism. Since energies of accelerated particles originate from the magnetic turbulence, taking into account the feedback (i.e., damping) of particle acceleration on the turbulence spectrum leads to a weaker magnetic field than was predicted in the standard afterglow dynamic model, given that the magnetic energy is consumed by particles. It also results in a particle spectrum softer than that predicted in the test-particle limit. Considering the fast mode of magnetosonic wave as the dominant particle scatterer and assuming the ISM for the circumburst environment, we found that protons can nevertheless be accelerated up to 10^{19} eV with a spectrum $dN/dE \propto E^{-1}$ for some favorable choices of a system's parameters. We also found that a pileup bump may occur in the spectrum ahead of the cutoff if the injection eddy scale is small, leading to a very hard particle spectrum with $dN/dE \propto E^0$. On the other hand, the maximum energy (or cutoff energy) of the accelerated protons is reduced because the maximum achievable energy in the acceleration is limited by the eddy scale.

An analytic estimate showed that ultrahigh-energy nuclei can easily survive photodisintegration in the early afterglows of GRBs, which implies that intermediate-mass or heavy nuclei can achieve 10^{20} eV in our model if they are loaded into GRB jets. Compared to the traditional model with acceleration by relativistic shocks, our model not only alleviates the energy budget problem but also provides a mechanism to generate the hard injection spectrum as required through explanation of the measured UHECRs spectra above the ankle and the chemical composition of UHECR as measured by the Pierre Auger Observatory.

ACKNOWLEDGMENTS

We thank the anonymous referee for the constructive report that improved the quality of this paper. We also acknowledge helpful discussions with Peter Mészáros, Katsuaki Asano, Huirong Yan, Joshi Jagdish and Jun Kakuwa. This work is supported by the National Key R&D program of China under the Grant No. 2018YFA0404203 and the NSFC Grants No. 11625312, No. 11851304, No. U2031105.

APPENDIX A: SKELETON PLOTS OF FIGURES 1, 2, AND 4

In order to illustrate that the damping of turbulent waves occurs not only around larger wave numbers but also smaller ones, we plot more moments for four different cases of the UHECR protons spectra and the turbulence spectra, as shown in Fig. 5. We can see that at a very early stage of the wave-particle system's evolution in cases I and II, the wave is damped by protons significantly around k_{inj}. This means that almost all of the turbulence energy is extracted by protons via gyroresonant interactions. This is also the reason why the magnetic field energy density in Fig. 3 drops much more quickly than in the other two cases.

From Fig. 5, we notice that the quasiperiodic fluctuation behavior around injection energy on the proton spectra and around the resonant injection wave number (sometimes at high wave numbers and sometimes at low wave numbers—even around the injection of waves k_{inj}) on the turbulence spectra. This behavior is caused by the resonant wave-particle interactions.

APPENDIX B: THE NUMBER OF PROTONS EVOLUTION

We now address the number of particles evolution in the jet's comoving frame in four different cases. The fluctuations on the curves are induced by the joint effects

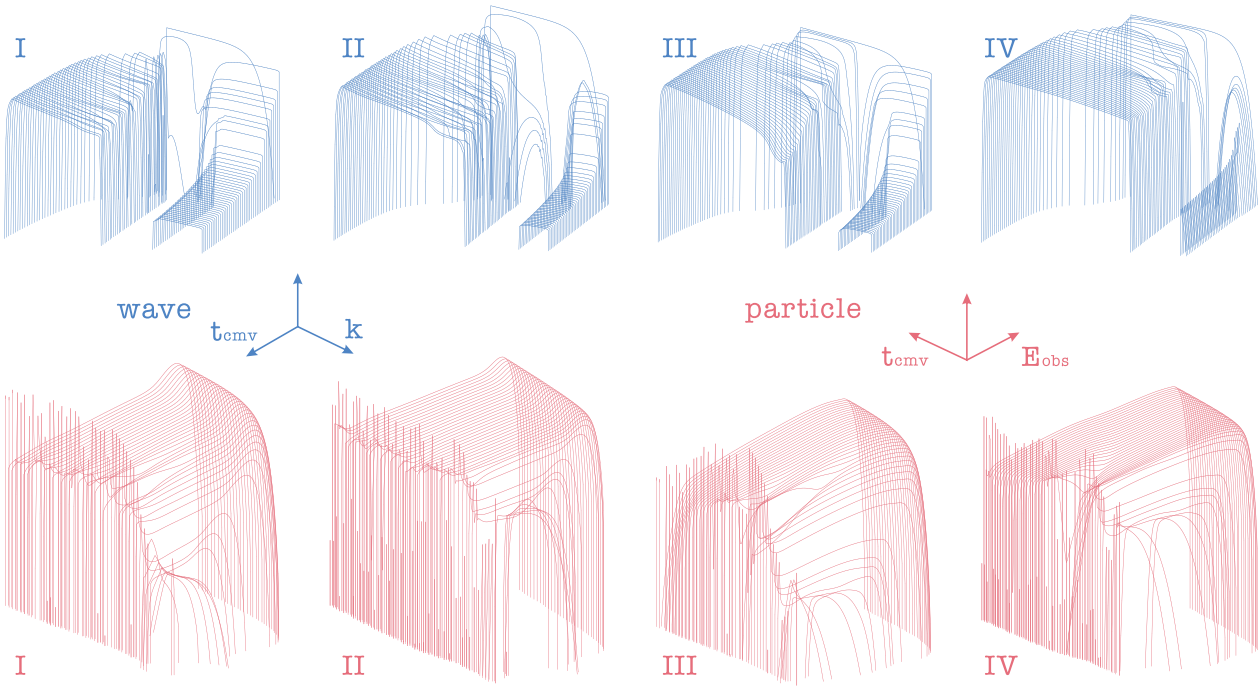

FIG. 5. Upper panels: four cases of turbulence spectral energy density spectra evolution. Lower panels: four cases of UHECR proton spectra evolution. The time vector of the triads represents the evolution direction.

of the wave-particle gyroresonant interactions, adiabatic cooling of turbulent magnetic fields and particle escape, as shown in Fig. 6. In the absence of particle escape, the number of particles continuously increase until the end of the evolution. However, in the case of particle escape (cases II–IV), the energized particles which extract energy from turbulent waves will escape from the acceleration region, causing the number of these particles to drop until about 100 s into the comoving frame. The reduction in particle number also reduces the damping rate. After awhile, the newly injected magnetic energy gradually increases to a certain amount which can keep dynamic quasiequilibrium with their adiabatic cooling and the damping of waves by particles until the bulk Lorentz factor Γ of the shock begins to drop significantly, as shown in the lower panels of Fig. 6. Owing to its high sensitivity to the variation of the value of Γ, the evolution of the nonlinear coupled FP equations enters the second dynamic equilibrium process. The multiplicity of the fluctuation of the number of particles evolution originates from the features of the logarithmic coordinate and the decline of Γ. An interpretation of the peculiarity of case I can be found in the bottom panels of Fig. 3 and in Appendix C.

APPENDIX C: THE INJECTION WAVE NUMBER k_{inj} VERSUS THE RESONANT INJECTION WAVE NUMBER $k_{res,inj}$

When $k_{inj} > k_{res,inj}$, the following condition should be met:

$$B\xi > \eta \equiv \frac{2\pi\Gamma E_{inj}}{eR}. \tag{C1}$$

In Fig. 3, we can see that the condition is well satisfied in cases II–IV. However, in case I, $k_{res,inj} = k_{inj}$ at a very early stage of evolution ($t_0 = 60$ s) for the first time in the jet's comoving frame. The value of η remains 0.0033 at the early stage of evolution. The initial value of $B\xi = B_0\xi \simeq 0.1844$ is larger than the value of η from the beginning of evolution until 60.6995 s. The damping of turbulent waves occurs around the injection wave number until $k_{res,inj} = k_{inj}$ again at around 223.5 s in the comoving frame, as shown in the bottom panels of Fig. 3. We know that the initial magnetic field $B_0 \propto n_{ISM}^{1/2}$ with $n_{ISM} = 0.01$ cm^{-3} and $\xi = 0.1$ in case I. As damping occurs at the injection scale, the magnetic fields drop quickly due to their adiabatic cooling and the damping of waves by particles. The value of $B\xi$ is more likely to become smaller than the value of η than in the other three cases. With the further injection of fast magnetosonic waves, the decline of the resonant wave number is very slow until $k_{res,inj} = k_{inj}$, again at $t_{cmv} = 223.5$ s. Actually, there are no turbulent waves to energize particles when $k_{res,inj} < k_{inj}$. Therefore, during the period spanning from $t_{cmv} = 60.6995$ s to $t_{cmv} = 223.5$ s, the injected particles do not accelerate to higher energy. Consequently, the number of particles remains unchanged, as shown in case I of Fig. 6 in Appendix B.

After the "step" transition (from $k_{res,inj} > k_{inj}$ to $k_{res,inj} < k_{inj}$ again) in case I, the newly injected magnetic energy

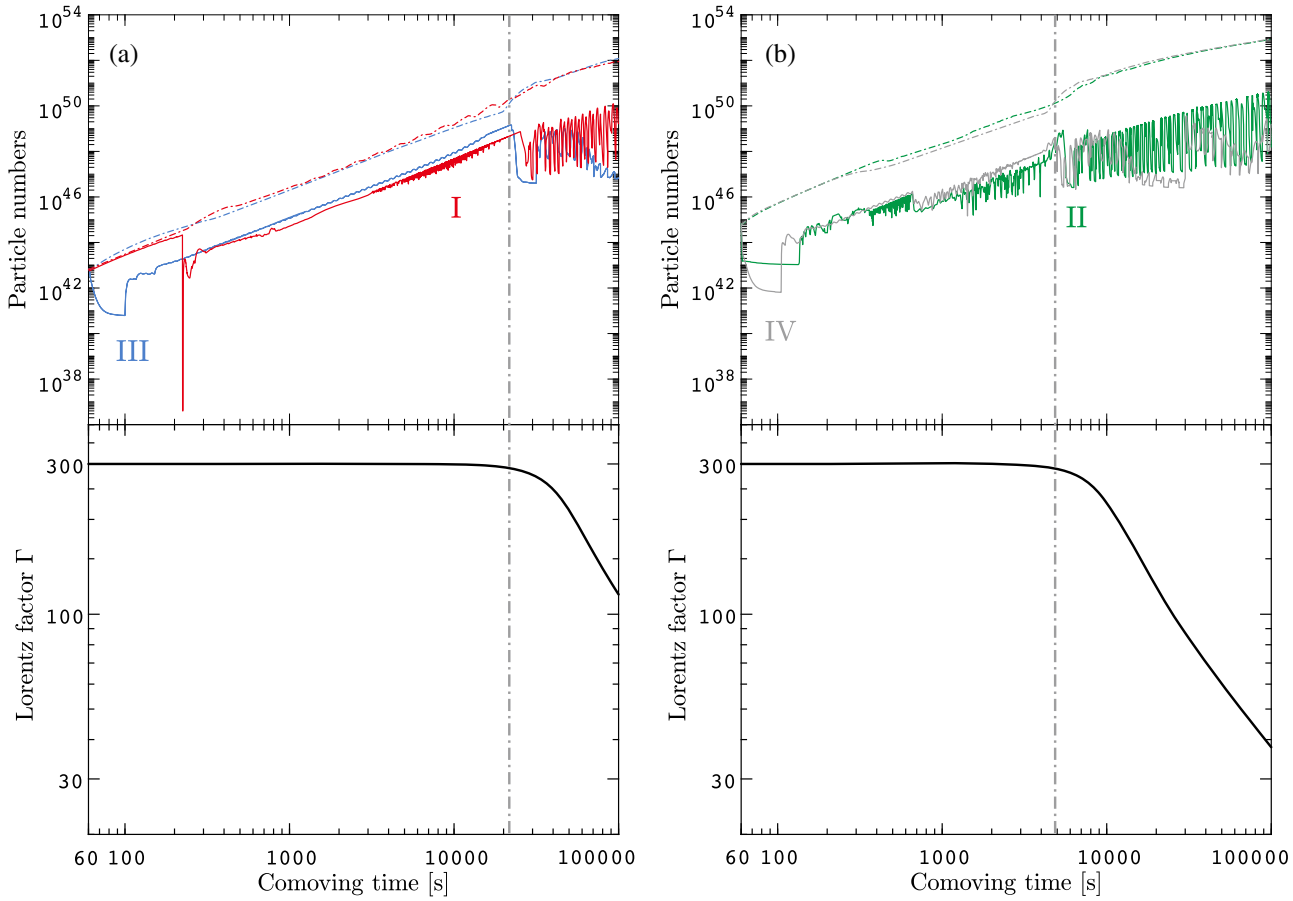

FIG. 6. Upper panels: amount of proton evolution in four different cases. The red lines illustrate case I, the blue lines illustrate case III, the green lines illustrate case II, and the gray lines illustrate case IV. The dash-dotted lines do not take the spatial escape effect into account, while the solid lines do. Lower panels: evolution of the bulk Lorentz factor Γ of the shock wave in the jet's comoving frame. Left panels: cases I and III. Right panels: cases II and IV. The vertical dash-dotted lines represent the moment when Γ starts to decrease significantly.

accumulates very quickly, resulting in a tiny bump at the moment. In the meantime, the accumulated particles can gain energy from turbulent waves via gyroresonant interactions again. Thus, the escape effect of the particles is significant within a very short period of time, as shown in Appendix B. This is also the reason for the nontrivial behaviors of the evolution of the magnetic field energy density and turbulence energy and cosmic-ray energy of case I in Fig. 3.

[1] A. Letessier-Selvon and T. Stanev, Rev. Mod. Phys. **83**, 907 (2011).
[2] J. Linsley, Phys. Rev. Lett. **10**, 146 (1963).
[3] L. A. Anchordoqui, Phys. Rep. **801**, 1 (2019).
[4] Pierre Auger Collaboration, Science **357**, 1266 (2017).
[5] R. Abbasi *et al.* (Telescope Array Collaboration), Astrophys. J. **862**, 91 (2018).
[6] P. L. Biermann and P. A. Strittmatter, Astrophys. J. **322**, 643 (1987).
[7] V. Berezinsky, A. Gazizov, and S. Grigorieva, Phys. Rev. D **74**, 043005 (2006).
[8] E. Waxman, Phys. Rev. Lett. **75**, 386 (1995).
[9] M. Vietri, Astrophys. J. **453**, 883 (1995).
[10] K. Murase, K. Ioka, S. Nagataki, and T. Nakamura, Astrophys. J. **651**, L5 (2006).
[11] X. Y. Wang, S. Razzaque, P. Mészáros, and Z. G. Dai, Phys. Rev. D **76**, 083009 (2007).
[12] R. Y. Liu and X. Y. Wang, Astrophys. J. **746**, 40 (2012).
[13] G. R. Farrar and A. Gruzinov, Astrophys. J. **693**, 329 (2009).
[14] B. T. Zhang, K. Murase, F. Oikonomou, and Z. Li, Phys. Rev. D **96**, 063007 (2017).

[15] D. Biehl, D. Boncioli, C. Lunardini, and W. Winter, Sci. Rep. **8**, 10828 (2018).
[16] C. A. Norman, D. B. Melrose, and A. Achterberg, Astrophys. J. **454**, 60 (1995).
[17] V. S. Berezinsky, P. Blasi, and V. S. Ptuskin, Astrophys. J. **487**, 529 (1997).
[18] G. Vannoni, F. A. Aharonian, S. Gabici, S. R. Kelner, and A. Prosekin, Astron. Astrophys. **536**, A56 (2011).
[19] J. Arons, Astrophys. J. **589**, 871 (2003).
[20] K. Kotera, Phys. Rev. D **84**, 023002 (2011).
[21] R. Schlickeiser and C. D. Dermer, Astron. Astrophys. **360**, 789 (2000), http://articles.adsabs.harvard.edu/pdf/1984A%26A...136..227S.
[22] R. Y. Liu, X. Y. Wang, and Z. G. Dai, Mon. Not. R. Astron. Soc. **418**, 1382 (2011).
[23] K. Asano and P. Mészáros, Phys. Rev. D **94**, 023005 (2016).
[24] B. T. Zhang, K. Murase, S. S. Kimura, S. Horiuchi, and P. Mészáros, Phys. Rev. D **97**, 083010 (2018).
[25] A. R. Bell, Mon. Not. R. Astron. Soc. **182**, 147 (1978).
[26] R. D. Blandford and J. P. Ostriker, Astrophys. J. **221**, L29 (1978).
[27] Y. A. Gallant and A. Achterberg, Mon. Not. R. Astron. Soc. **305**, L6 (1999).
[28] M. Lemoine, G. Pelletier, and B. Revenu, Astrophys. J. **645**, L129 (2006).
[29] A. Marcowith, G. Ferrand, M. Grech, Z. Meliani, I. Plotnikov, and R. Walder, Living Rev. Comput. Astrophys. **6**, 1 (2020).
[30] B. Katz, R. Budnik, and E. Waxman, J. Cosmol. Astropart. Phys. 03 (2009) 020.
[31] E. Waxman, arXiv:1010.5007.
[32] P. Baerwald, M. Bustamante, and W. Winter, Astropart. Phys. **62**, 66 (2015).
[33] J. Bednarz and M. Ostrowski, Phys. Rev. Lett. **80**, 3911 (1998).
[34] A. Achterberg, Y. A. Gallant, J. G. Kirk, and A. W. Guthmann, Mon. Not. R. Astron. Soc. **328**, 393 (2001).
[35] M. Lemoine and G. Pelletier, Astrophys. J. **589**, L73 (2003).
[36] U. Keshet and E. Waxman, Phys. Rev. Lett. **94**, 111102 (2005).
[37] M. G. Aartsen *et al.* (IceCube Collaboration), Astrophys. J. **843**, 112 (2017).
[38] R. Alves Batista *et al.*, Front. Astron. Space Sci. **6**, 23 (2019).
[39] R. Alves Batista, R. M. de Almeida, B. Lago, and K. Kotera, J. Cosmol. Astropart. Phys. 01 (2019) 002.
[40] R. Schlickeiser, Astron. Astrophys. **136**, 227 (1984), http://articles.adsabs.harvard.edu/pdf/2000A%26A...360..789S.
[41] P. A. Becker, T. Le, and C. D. Dermer, Astrophys. J. **647**, 539 (2006).
[42] Ł. Stawarz and V. Petrosian, Astrophys. J. **681**, 1725 (2008).
[43] J. Cho and A. Lazarian, Phys. Rev. Lett. **88**, 245001 (2002).
[44] H. Yan and A. Lazarian, Phys. Rev. Lett. **89**, 281102 (2002).
[45] K. D. Makwana and H. Yan, Phys. Rev. X **10**, 031021 (2020).
[46] V. N. Tsytovich, *An Introduction to the Theory of Plasma Turbulence* (Pergamon Press, Oxford, 1972).
[47] P. C. Duffell and A. I. MacFadyen, Astrophys. J. **775**, 87 (2013).
[48] J. Matsumoto and Y. Masada, Astrophys. J. **772**, L1 (2013).
[49] W. Zhang, S. E. Woosley, and A. I. MacFadyen, Astrophys. J. **586**, 356 (2003).
[50] H. Yan and A. Lazarian, Astrophys. J. **614**, 757 (2004).
[51] R. M. Kulsrud, *Plasma Physics for Astrophysics* (Princeton University Press, Princeton, NJ, 2005).
[52] J. Steinacker and J. A. Miller, Astrophys. J. **393**, 764 (1992).
[53] Y. Zhou and W. H. Matthaeus, J. Geophys. Res. **95**, 14881 (1990).
[54] H. Yan and A. Lazarian, Astrophys. J. **673**, 942 (2008).
[55] Y. Teraki and K. Asano, Astrophys. J. **877**, 71 (2019).
[56] Y. F. Huang, Z. G. Dai, and T. Lu, Mon. Not. R. Astron. Soc. **309**, 513 (1999).
[57] E. Fermi, Phys. Rev. **75**, 1169 (1949).
[58] D. B. Melrose, Astrophys. Space Sci. **2**, 171 (1968).
[59] D. B. Melrose, *Plasma Astrophysics: Nonthermal Processes in Diffuse Magnetized Plasmas* (Gordon and Breach Science Publishers, New York, 1980), Vol. 1.
[60] V. Petrosian and S. Liu, Astrophys. J. **610**, 550 (2004).
[61] A. Tramacere, E. Massaro, and A. M. Taylor, Astrophys. J. **739**, 66 (2011).
[62] J. W. Lynn, E. Quataert, B. D. G. Chandran, and I. J. Parrish, Astropart. Phys. **791**, 71 (2014).
[63] J. Kakuwa, Astrophys. J. **816**, 24 (2016).
[64] B. Zhang, *The Physics of Gamma-Ray Bursts* (Cambridge University Press, Cambridge, England, 2018).
[65] P. Mertsch, J. Cosmol. Astropart. Phys. 12 (2011) 010.
[66] D. Eichler, Astrophys. J. **229**, 413 (1979).
[67] J. A. Miller, T. N. Larosa, and R. L. Moore, Astrophys. J. **461**, 445 (1996).
[68] G. Brunetti and A. Lazarian, Mon. Not. R. Astron. Soc. **378**, 245 (2007).
[69] R. Y. Liu, F. M. Rieger, and F. A. Aharonian, Astrophys. J. **842**, 39 (2017).
[70] P. Kumar and R. Barniol Duran, Mon. Not. R. Astron. Soc. **409**, 226 (2010).
[71] R. Y. Liu and X. Y. Wang, Astrophys. J. **730**, 1 (2011).
[72] M. Lemoine, Z. Li, and X. Y. Wang, Mon. Not. R. Astron. Soc. **435**, 3009 (2013).
[73] F. Samuelsson, D. Bégué, F. Ryde, A. Pe'er, and K. Murase, Astrophys. J. **902**, 148 (2020).
[74] K. Asano and T. Terasawa, Mon. Not. R. Astron. Soc. **454**, 2242 (2015).
[75] F. W. Stecker, Phys. Rev. Lett. **21**, 1016 (1968).
[76] J. L. Puget, F. W. Stecker, and J. H. Bredekamp, Astrophys. J. **205**, 638 (1976).
[77] S. Karakula and W. Tkaczyk, Astropart. Phys. **1**, 229 (1993).
[78] P. Mészáros, Rep. Prog. Phys. **69**, 2259 (2006).
[79] X. Y. Wang, S. Razzaque, and P. Mészáros, Astrophys. J. **677**, 432 (2008).
[80] V. A. Acciari, S. Ansoldi, L. A. Antonelli, A. A. Engels, D. Baack, A. Babić *et al.* (MAGIC Collaboration), Nature (London) **575**, 459 (2019).
[81] A. M. Hillas, Annu. Rev. Astron. Astrophys. **22**, 425 (1984).